*metals*

MDPI

*Article*

# Cr-Co Oxide Coatings Resistant to Corrosion, Electrodeposited on 304 SS Using an Ethylene Glycol-Water Solvent

**Carmen E. Velázquez-González, Francisco J. Martínez-Baltodano, Jorge López-Cuevas * and Gregorio Vargas-Gutiérrez ***

Cinvestav-Saltillo, Avenida Industria Metalúrgica #1062, Parque Industrial Saltillo-Ramos Arizpe, Ramos Arizpe 25900, Mexico; carmen.velazquez@cinvestav.edu.mx (C.E.V.-G.); fco.mtzbaltodano@cinvestav.edu.mx (F.J.M.-B.)

* Correspondence: jorge.lopez@cinvestav.edu.mx (J.L.-C.); gregorio.vargas@cinvestav.mx (G.V.-G.)

**Abstract:** The electrochemical co-deposition of Cr-Co oxide coatings at room temperature on 304 stainless steel (SS) was studied using an electrolyte composed of a mixture of ethylene glycol (EG), hydrated metal chloride salts ($MCln{\cdot}YH_2O$), and water as a secondary hydrogen donor (HBD). Metallic Cu and Ni undercoats were applied to improve the adhesion of a posterior Cr-Co metallic and oxide layer. The electroactive events that took place during both electrodeposition processes were studied using cyclic voltammetry (CV) and chronoamperometry. The microstructure and composition of the surface layers were studied using scanning electron microscopy (SEM/EDS), X-ray diffraction (XRD) and cross-sectional elemental mapping via transmission electron microscopy (TEM). The surface of steel with the Cr-Co:EG-$H_2O$ coating showed greater resistance to pitting corrosion (123.93 mV) compared to untreated stainless steel (62.3 mV). This sample showed a large hystere-sis area, which is associated with high resistance to pitting corrosion by the occurrence of a re-passivation of the sample at a Erep value of 24.31 mV. After the cyclic potentiodynamic polariza-tion (CPP) test, the lowest specific mass loss (0.001 mg/cm$^2$) was achieved for the AISI 304 SS sample coated using EG-water solvents (Cr-Co:EG-$H_2O$), while the untreated AISI 304 SS reached a higher specific mass loss (0.01 mg/cm$^2$). The Electrochemical Impedance Spectroscopy (EIS) tests showed that the uniform corrosion resistance varied significantly from the untreated AISI 304 SS (35 kΩ) to the coated sample (57 kΩ), which is attributed to the protection provided by the chromium and cobalt oxides coating. The best corrosion resistance achieved was correlated with a superhydrophobic character (with a contact angle of 158.41°) of the Cr-Co coatings. This was in turn a consequence of a needle-like morphology characteristic of these oxides.

**Keywords:** ethylene glycol-water solvent; Cr-Co oxide coatings; corrosion

check for updates

**Citation:** Velázquez-González, C.E.; Martínez-Baltodano, F.J.; López-Cuevas, J.; Vargas-Gutiérrez, G. Cr-Co Oxide Coatings Resistant to Corrosion, Electrodeposited on 304 SS Using an Ethylene Glycol-Water Solvent. *Metals* **2024**, *14*, 77. https://doi.org/10.3390/met14010077

Academic Editors: Marcello Cabibbo and Belén Díaz Fernández

Received: 4 July 2023
Revised: 15 September 2023
Accepted: 19 September 2023
Published: 9 January 2024

**Copyright:** © 2024 by the authors. Licensee MDPI, Basel, Switzerland. This article is an open access article distributed under the terms and conditions of the Creative Commons Attribution (CC BY) license (https://creativecommons.org/licenses/by/4.0/).

## 1. Introduction

Electrodeposition research carried out recently has been focused on the use of deep eutectic solvents (DESs), particularly of type III, due to their high solubility for metal salts, electrochemical stability, and wide potential window compared to aqueous solutions [1–5]. Ethaline (Figure 1a), which is composed of choline chloride (ChCl) as a hydrogen bond acceptor (HBA) and ethylene glycol (EG) as a hydrogen donor (HBD), is one of the most common DESs used [6]. However, recent electrodeposition works [7–9] have proposed the elimination or replacement of HBAs from ethaline (Figures 1b and 1c, respectively) due to their aggressiveness towards the substrates and coatings. This has led to the development of EG-based solvents, thus favoring simpler and cheaper electrodeposition procedures. However, the number of successful metallic deposits that have been obtained via electrodeposition using this kind of solvent is limited to a few metals such as Zn, Co, Cr, Sn, and Cu [10–14]. In other areas, investigations have succeeded in decreasing the rate of corrosion by employing a mixture of ethylene glycol and water as an automotive coolant, in the presence of inhibitors [15,16].

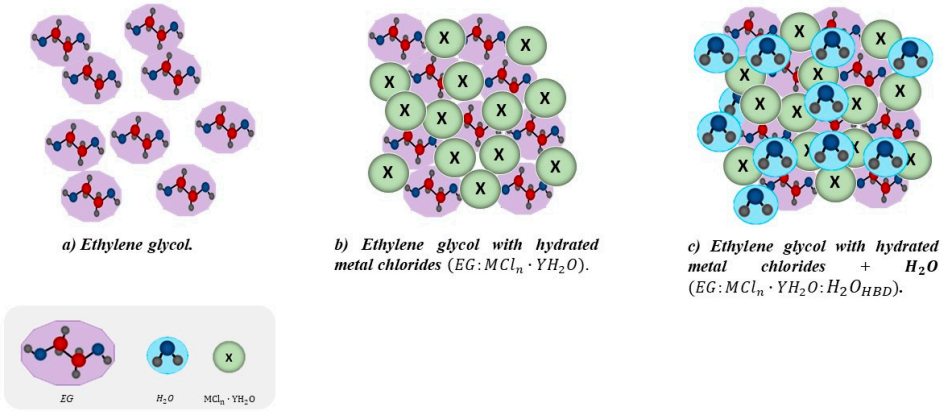



**Figure 1.** (**a**–**c**) Formation sequence of electrolytes based on ethylene glycol-hydrated salts and water.

In Figure 1c, this EG-based electrolyte is represented by the general formula EG:MCln·$YH_2O$, where M is the precursor metal to be deposited and Y represents the degree of hydration of the metal chloride salt. To date, the electrodeposition of metal oxides utilizing EG-based solvents has not been thoroughly investigated.

In this work, we present an innovative approach for the electrodeposition of a thin layer of Cr-Co oxides, using the new solvent composition depicted in Figure 1c, represented by the general formula EG:MCln·$YH_2O$:$H_2O_{HBD}$. This solvent composition was obtained by adding up to 30 wt% of $H_2O$ as a secondary HBD. Our main objective was to overcome the limitations related to the low solubility of metal precursor salts and the reduced electrical conductivity of EG-based solutions. As a first step, metallic layers of Cu and Ni were successively electrodeposited on the surface of the 304 SS to create an undercoat that acted as a "primer" to enhance the adhesion of a posterior Cr-Co oxide layer.

The marine environment is one of the most aggressive that exist due to its corrosivity towards steels and other metals [17,18], which is related to a pitting corrosion in materials exposed to this environment. It is known that Cr-Co coatings provide a substrate with general corrosion and wear resistance [19]. One objective of the present study was to confirm that a Cr-Co oxide layer electrodeposited in a mixture of EG-water improves the anti-pitting property of AISI 304 SS. The use of EG-water solvents has led to the development of simpler and cheaper electrodeposition procedures. Furthermore, the electrodeposition of metal oxides using EG-water solvents has not yet been thoroughly investigated.

## 2. Materials and Methods

The electrochemical study of the electroactive events that took place during electrodeposition was carried out using cyclic voltammetry (CV) and chronoamperometry. The microstructure of the coatings produced was analyzed via scanning electron microscopy (SEM), energy dispersive spectroscopy (EDS), X-ray diffraction (XRD) analysis, and cross-section composition by means of elemental mapping in a transmission electron microscope (TEM).

Prior to the electrodeposition of the metallic Cu and Ni undercoat, the surface of the 304 SS was sandblasted. This operation was carried out by repeatedly impacting the surface of the substrate with hard particles of ceramic materials. For this, an NSKI Twin-Pen Sandblaster [20] was used, 304 SS discs of 1 $cm^2$ were employed as substrates, and silica particles were projected for 5 s at a pressure of 60 psi. Sandblasted surfaces promote the adhesion of subsequent coatings [21]. Figure 2 illustrates the procedure followed to produce the Cr-Co oxide coatings.

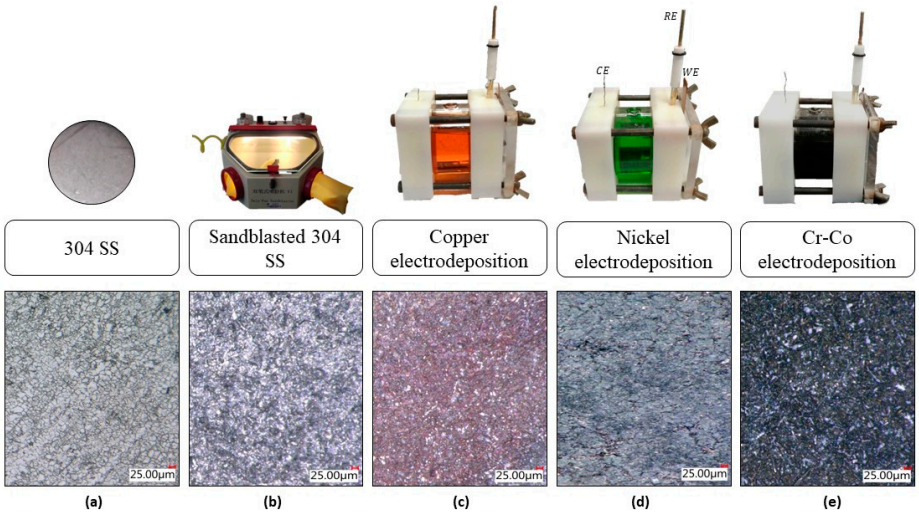



**Figure 2.** Procedure followed to produce Cr-Co oxide coatings. (**a**) As-received 304 SS, (**b**) sandblasted 304 SS, (**c**) metallic Cu undercoat, (**d**) metallic Ni undercoat, and (**e**) metallic and oxide Cr-Co black coating.

The coatings shown in Figure 2 were obtained via electrodeposition using the chronoamperometry technique in a 25 milliliter glass electrochemical cell with a 3-electrode configuration (platinum counter electrode, working electrode (substrate to be coated) and $Ag/Ag^+$ non-aqueous reference electrode). The separation between the working electrode and the counter electrode was 5 cm. A PARSTAT MC PMC-1000 potentiostat (AMETEK$^{TM}$ Scientific Instruments, Oak Ride, TN, USA) was used as a power supply. The electrodeposit time was set at 15 min at room temperature for all coatings. Table 1 specifies the composition of the solvents used for each electrodeposition process. Analytical grade Sigma-Aldrich (Darmstadt, Germany) reagents were used. The metallic Cu deposit was obtained using the electrolyte EG:0.1Cu $Cl_2{\cdot}2H_2O$, while the metallic Ni deposit was obtained using the electrolyte EG:0.1$NiCl_2{\cdot}6H_2O$. For the co-deposition of Cr-Co metals and oxides, the electrolyte 3EG:0.1$CrCl_3{\cdot}6H_2O$ + 0.2$CoCl_2{\cdot}6H_2O$:$H_2O_{HBD}$ was used. Deionized water was used as a secondary HBD. A 3:1 molar ratio was used for the solvent EG:$H_2O_{HBD}$, with total amount of $H_2O$ of 25 wt%, including the hydration water of the precursor salts. This was the optimal amount of water in the mixture because it allowed water molecules to be incorporated into the EG intermolecular network without modifying the solvent nanostructure [22].

**Table 1.** Composition of EG-based electrolytes.

| Coating | Electrolyte | | | |
|---|---|---|---|---|
| Metallic Cu | EG:0.1$CuCl_2{\cdot}2H_2O$ | | | |
| | EG | | $CuCl_2{\cdot}2H_2O$ | 0.1 M |
| Metallic Ni | EG:0.1$NiCl_2{\cdot}6H_2O$ | | | |
| | EG | | $NiCl_2{\cdot}6H_2O$ | 0.1 M |
| Cr-Co (Metallic and oxides) | EG:0.1$CrCl_3{\cdot}6H_2O$ + 0.2$CoCl_2{\cdot}6H_2O$ | | | |
| | EG | | $CrCl_3{\cdot}6H_2O$:$CoCl_2{\cdot}6H_2O$ | 0.1:0.2 M |
| | 3EG:0.1$CrCl_3{\cdot}6H_2O$ + 0.2$CoCl_2{\cdot}6H_2O$:$H_2O_{HBD}$ | | | |
| | EG:$H_2O_{HBD}$ | 3:1 M | $CrCl_3{\cdot}6H_2O$:$CoCl_2{\cdot}6H_2O$ | 0.1:0.2 M |

The surface analysis of the coatings was carried out using a JSM-7800F PRIME Schottky field-emission scanning electron microscope (SEM) (Jeol Ltd., Tokyo, Japan), which was operated at an acceleration voltage of 5 kV, using secondary electrons and a working distance of 10 mm. The composition of the phases was determined using a Philips XL30 ESEM apparatus equipped with an EDAX Genesis EDS microanalysis system (FEI

Technology, Eindhoven, Netherlands), which was operated at an acceleration voltage of 20 kV. The crystalline phases formed on the surface of the substrates were identified via X-ray diffraction (XRD) using a Bruker AXS D8 diffractometer (Advance™, Karlsruhe, Germany) diffractometer operated under the following conditions: CuKα radiation, voltage of 40 kV, current of 30 mA, scanning 2θ range of 20–80°, and aperture of 0.02°. To perform cross-sectional analysis of the coatings, high-quality TEM (transmission electron microscope) lamellae were prepared for each coating using the gallium ion beam in the FEI Scios DualBeam system (SEM/focused ion beam (FIB) system) (Thermo Fisher Scientifics, Eindhoven, The Netherlands). This allowed the composition of the layers to be analyzed using elemental mapping using the Thermo Scientific AutoTEM 5 software package (DualBeam™, Eindhoven, The Netherlands; https://www.thermofisher.com/mx/es/home/electron-microscopy/products/software-em-3d-vis/autotem-5-software.html (accessed on 18 September 2023)).

Contact angle and free surface energy for ultra-pure water on the surface of the coatings were evaluated using a Xiangyi SI-CAM2000D (LABFREEZ™ Instrument Group Co., Ltd., Guangzhou, China) enhanced contact angle meter.

Corrosion measurements in simulated seawater were carried out by cyclic potentiodynamic polarization (CPP) and Electrochemical Impedance Spectroscopy (EIS) tests. In both tests, a Ag/AgCl aqueous reference electrode and simulated seawater were used. Simulated seawater was prepared according to the ISO 11130 standard [23]. Table 2 specifies the composition of the simulated seawater used.

**Table 2.** Simulated seawater composition used, according to the ISO 11130 standard; pH was adjusted to a value of 8.2 using a 0.1 N NaOH solution.

| Chemical Components | Concentration (g/L) | Composition (wt%) |
|---|---|---|
| NaCl | 30.67 | 58.46 |
| $Na_2SO_4$ | 5.12 | 9.70 |
| $MgCl_2{\cdot}6H_2O$ | 13.89 | 26.48 |
| $CaCl_2$ | 1.45 | 2.76 |
| $SrCl_2{\cdot}6H_2O$ | 0.05 | 0.10 |
| KCl | 0.87 | 1.66 |
| $NaHCO_3$ | 0.25 | 0.48 |
| KBr | 0.13 | 0.24 |
| $H_3BO_3$ | 0.03 | 0.06 |
| NaF | 0.005 | 0.01 |

To evaluate the pitting corrosion resistance of an untreated AISI 304 SS specimen and a coated sample Cr-Co:EG-$H_2O$, a CPP analysis was performed according to the ASTM standard G61-86 (Reapproved 2018) [24], using a Parstat MC potentiostat from Ametec™. The electrolyte was purged with nitrogen for 1 h to remove dissolved oxygen. After purging, the electrolyte remained in OCP mode for 50 min. The scan started at the corrosion potential (Ecorr) and it was performed in the direction of the anodic potential at a rate of 0.6 V/h, the exploration direction was reversed on reaching 1.20 V or when a current of 5 mA was reached.

Due to the nature and chemical composition of the coatings (chromium and cobalt oxides with a needle-like morphology), the Tafel method is not applicable for estimating the uniform corrosion rate. An alternative method that can be used for this is the EIS method. Thus, the assessment of general corrosion resistance was conducted using this technique using a AutoLab potentiostat (Metrohm Autolab S.V™, Utrecht, The Netherlands). The INTELLO 1.2 software (Metrohm Autolab S.V™, Utrecht, The Netherlands) was employed to acquire Nyquist impedance spectra within a frequency range of 100,000 to 0.0001 Hz,

utilizing a voltage amplitude of 5 mV and capturing 10 points per frequency decade. The analysis of impedance values derived from Nyquist plot fitting and equivalent electrical circuits was conducted using Nova 2.1 software (Metrohm Autolab S.V$^{TM}$, Utrecht, The Netherlands).

## 3. Results

### *3.1. Electrochemical Study*

The electrochemical behavior of the EG-based electrolytes EG:MCln·$YH_2O$ and EG:$MCl_n$·$YH_2O$:$H_2O_{HBD}$ was studied, identifying via cyclic voltammetry (CV) the electroactive events within the reduction region necessary for the electrodeposition of metals. All CV curves in Figure 3 start from the open circuit potential (OCP) of the system used in each case, with a left-to-right potential sweep, in the range 1.50–2.50 V. Figure 3a shows the CV curve obtained for the surface of sandblasted 304 SS and EG, which is considered as an electrochemical reference, and confirms the absence of electroactive events that interfere with the reduction of the hydrated precursor salts during subsequent CV tests. The reduction zone in the CV curve of Figure 3b corresponds to the electrodeposition of metallic Cu on the surface of sandblasted 304 SS with EG and hydrated Cu (II) chloride salt, which requires two reduction stages to reach the Cu (0) metallic state. The first reduction, $R_1$ in Figure 3b, takes place in the range −0.25 to −1.00 V, and corresponds to a change from Cu (II) to Cu (I) oxidation states, while the second reduction event, $R_2$ in the range −1.25 to −2.00 V, corresponds to a change from Cu (I) to Cu (0) oxidation states. Once the metal reduction zone of Cu, $R_2$, was identified, chronoamperometry was used to determine the optimal value of electrical potential to produce a Cu coating with greater uniformity. The best metallic Cu coating obtained at −1.25 V, which is denoted as the Cu coating, was used as a working electrode in the Ni CV curve of Figure 3c, in conjunction with EG and hydrated Ni (II) chloride salt. The Ni precursor presents a single change from Ni (II) to Ni (0) oxidation states, so that a single reduction zone $R_1$ was obtained in the range −1.25 to −1.75 V. When evaluating the single metallic Ni reduction zone via chronoamperometry, the optimal electrical potential was expected to be preferentially close to the reduction peak (approximately −1.50 V). This was confirmed by obtaining the metallic Ni coating with the greatest uniformity by applying an electrical potential of −1.40 V.

Using Ni as a working electrode, the CV curves of Cr and Co in Figure 3d allow the identification of the reduction zones occurring during the co-deposition of Cr-Co at a 1:2 molar ratio, with EG:$H_2O_{HBD}$ at a 3:1 molar ratio, and hydrated Cr (III) and Co (II) chloride salts. The Cr precursor requires two changes in oxidation state before reaching the Cr (0) metallic state [25], and the Co precursor requires a single change in oxidation state to reach the Co (0) metallic state [26], which can be seen in the reduction regions in the CV curve in Figure 3d. In the first reduction zone, $R_1$, in the range 0.10 to −0.40 V, only a change from Cr (III) to Cr (II) oxidation states occurs, while in the second reduction zone, $R_2$, in the range −0.75 to −1.15 V, a second reduction from Cr (II) to Cr (0) and a direct reduction from Co (II) to Co (0) oxidation states happen simultaneously. According to the VC results, $R_2$ is defined as the reduction zone at which Cr and Co co-deposit, with preferential nucleation of Co due to its greater nobility.

Because the coatings were obtained sequentially, layer by layer, after the identification by CV of the metallic reduction interval for each coating, chronoamperometry became the criterion of selection of the electrical potential to produce the greatest uniformity in the coatings. Figure 4 shows the chronoamperometry curves that produced the best coatings for each of the three electrodepositions: Cu at −1.25 V, Ni at −1.40 V, and co-deposition of Cr-Co at an electrical potential of −1.00 V. All current transients of the chronoamperometry curves in Figure 4 showed a maximum current ($j_m$) that is characteristic of a typical nucleation process [27,28]. Therefore, the maximum current for the Cu electrodeposition was obtained at 141 s, for the Ni electrodeposition it was obtained at 120 s, and for the Co-Cr electrodeposition it was obtained at 60 s. As the number of coating layers increases, the amperometry curves tend to shift on the vertical axis due to the increased electrical resistance.

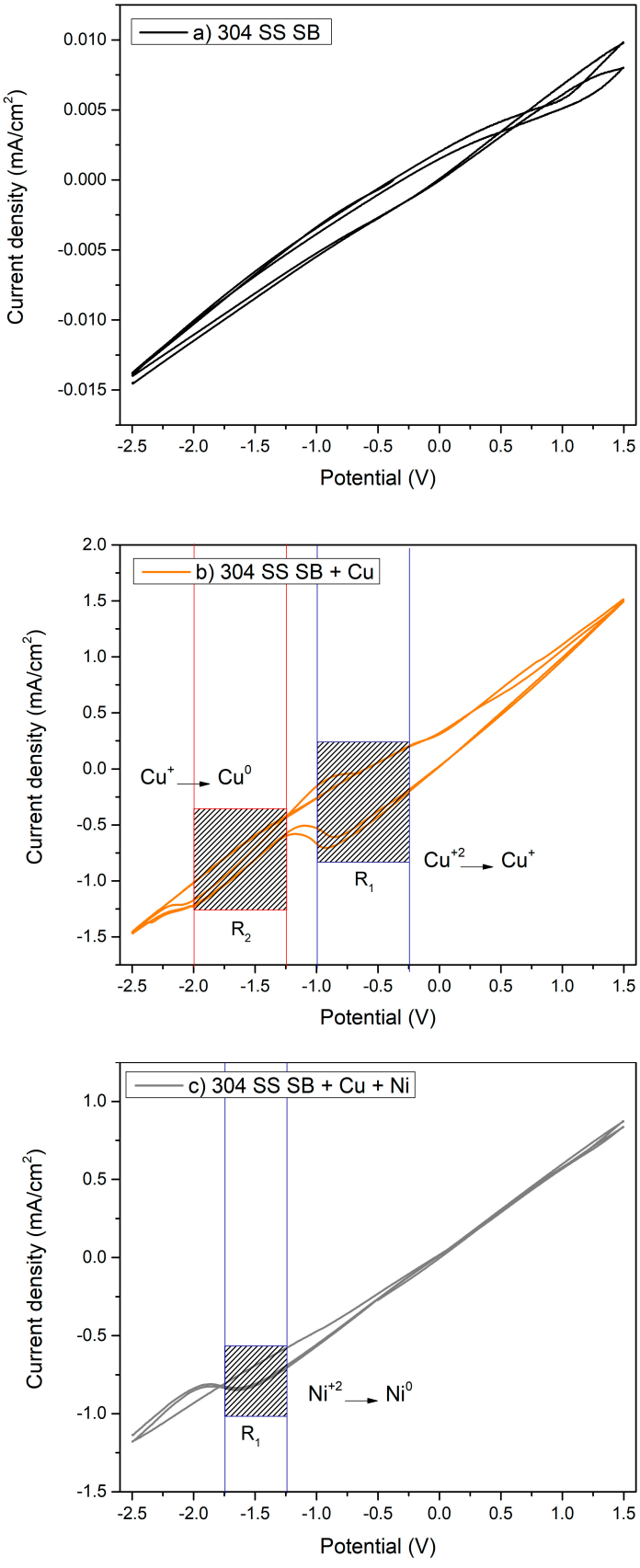



**Figure 3.** *Cont.*

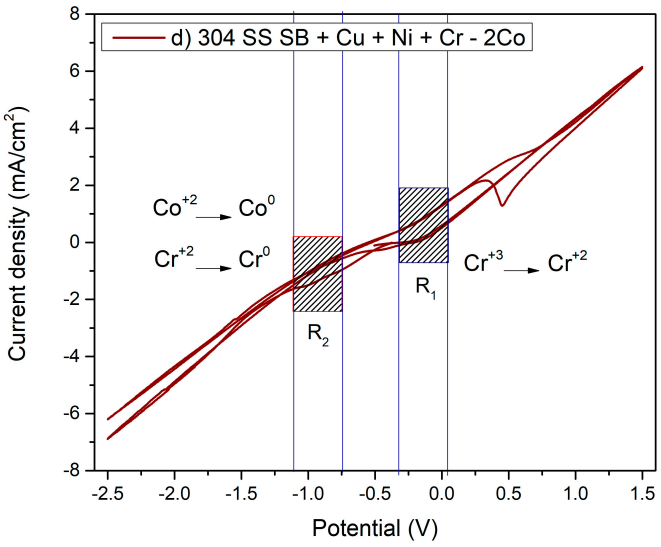



**Figure 3.** Cyclic voltammetry curves and identification of reduction zones for (**a**) sandblasted 304 SS in the presence of EG, (**b**) sandblasted 304 SS in the presence of EG and hydrated Cu (II) chloride salt, (**c**) Cu coating in the presence of EG and hydrated Ni (II) chloride salt, and (**d**) coating of Ni in the presence of EG:$H_2O_{HBD}$ with a 3:1 molar ratio, and hydrated Cr (III) and Co (II) chloride salts at a 1:2 molar ratio.

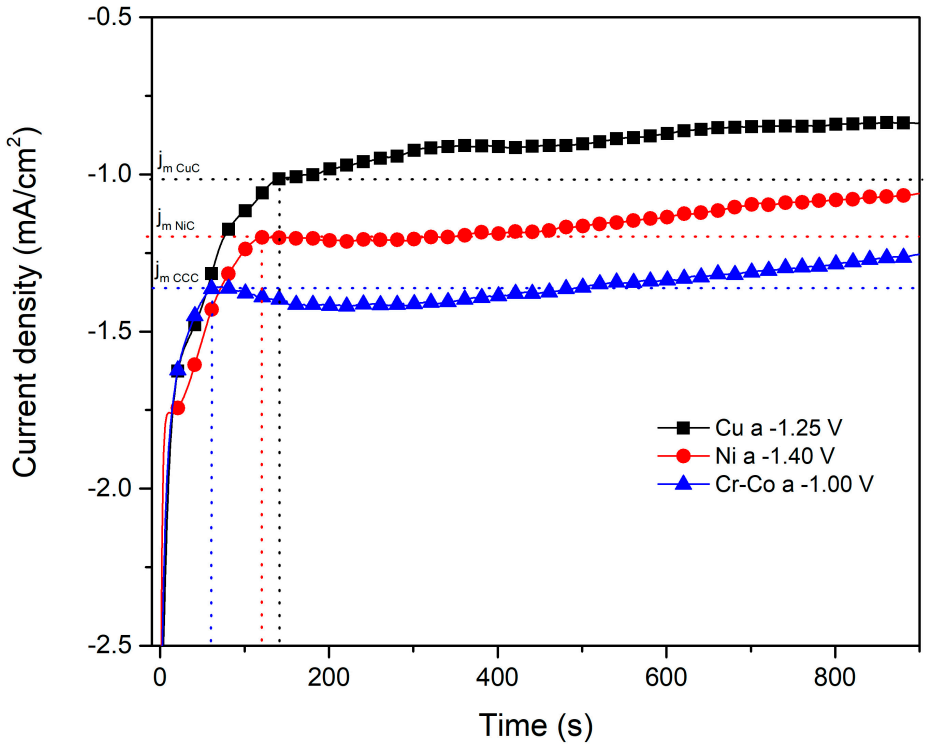



**Figure 4.** Chronoamperometry curves for Cu at −1.25 V (black squares) on sandblasted 304 SS in the presence of EG and hydrated Cu (II) chloride salt; Ni at −1.40 V (red circles) on Cu in the presence of EG and hydrated Ni (II) chloride salt, and Cr-Co at −1.00 V (blue triangles) on Ni in the presence of EG:$H_2O_{HBD}$ at a 3:1 molar ratio and hydrated Cr (III) and Co (II) chloride salts at a 1:2 molar ratio.

In this electrochemical study, the ability of the electrolyte EG:$MCl_n \cdot YH_2O$ to produce Cu and Ni coatings was demonstrated, identifying the regions of metal reduction by CV, and studying the process of nucleation of coatings by chronoamperometry, applying the optimal electrical potential determined from the CV study. It was also ensured that metallic coatings were obtained using the potential corresponding to the metal reduction region

during the electrodeposition process. Previous studies have demonstrated that using EG-based electrolytes can result in the deposition of Cu alloy coatings, as well as pure metallic Ni, but only on substrates other than 304 SS [29,30].

As in the case of electrolyte EG:MCln·$YH_2O$, the EG-based electrolyte EG:$MCl_n \cdot YH_2O$:$H_2O_{HBD}$ is considered to be suitable for producing Cr-Co metallic coatings. The above, in addition to the presence of oxides of both metals in these coatings, was corroborated via surface characterization carried out using SEM/EDS and XRD.

### 3.2. Surface Analysis of Coatings

Table 3 presents the elemental composition of Cu, Ni, and Cr-Co coatings determined via SEM/EDS. The composition of 304 SS without any preparation or surface treatment is presented as a reference. After sandblasting the surface of 304 SS, its oxygen and silicon surface content is increased due to the incrustation of silica particles during sandblasting. However, the Fe and Cr surface content decreases due to the removal of material caused by the repetitive impact by $SiO_2$ particles during sandblasting. After the application of the Cu coating, the surface content of Cu increases significantly, as expected. However, the detection of considerable amounts of the elements Fe, Cr, O, and Si indicates that the surface is not completely coated with Cu, or that this coating is very thin, so the alloying elements and the embedded $SiO_2$ particles present in the sandblasted 304 SS substrate are being detected. Table 3 shows that the Ni coating is predominantly composed of Ni, together with a relatively small amount of Fe, Cr, and Cu, indicating that this coating is more uniform than the previous one. Finally, the Cr-Co coating has a considerable content of Co, oxygen, and Cr, in addition to lower amounts of Ni, Fe, and Cu, as well as traces of Cl and Si. This can be attributed to the formation of oxides, and possibly also hydroxides, of Co and Cr on the surface of the substrate, because of the interaction of water present in the solvent as a secondary HBD with Cr and Co during the electrodeposition process. This was subsequently confirmed via XRD analysis and elemental mapping of the cross-section of the coatings. The Cr-Co coating was also analyzed using SEM/EDS.

**Table 3.** Analysis via EDS (in wt%) of 304 SS (304 SS), sandblasted 304 SS (304 SS SB), Cu over 304 SS SB, Ni over Cu, and Cr-Co over Ni.

| | 304 SS | 304 SS SB | Cu EG | Ni EG | Cr-Co EG:$H_2O$ | Cr-Co EG |
|---|---|---|---|---|---|---|
| | | | −1.25 V | −1.40 V | −1.00 V | −1.00 V |
| O k | 5.15 | 9.63 | 6.54 | 6.74 | 27.84 | 13.83 |
| Si k | 0.75 | 8.36 | 5.36 | 5.08 | 0.54 | 6.95 |
| Cl k | 0.10 | 0.08 | 0.30 | 0.12 | 0.57 | 0.64 |
| Cr k | 16.79 | 15.04 | 10.16 | 6.14 | 17.79 | 9.39 |
| Mn k | 1.19 | 1.14 | 0.85 | 0.62 | 0.38 | 0.39 |
| Fe k | 67.23 | 57.95 | 35.09 | 21.97 | 5.98 | 17.39 |
| Co k | 0.26 | 0.38 | 0.37 | 0.47 | 34.38 | 4.47 |
| Ni k | 7.88 | 6.89 | 3.77 | 48.27 | 8.05 | 38.89 |
| Cu k | 0.65 | 0.53 | 37.56 | 10.59 | 4.47 | 8.05 |

Improvement in coating uniformity can be achieved by replacing the base surface conditioning process, which involves sandblasting, with alternative methods such as traditional mechanical polishing or plasma electropolishing. These methods allow us to obtain flat surfaces, free of irregularities, as well as unwanted particles.

XRD analysis was performed to identify the phases present in the coatings obtained via electrodeposition. Figure 5 shows the XRD patterns obtained for 304 SS, 304 SS SB, Cu, Ni, and Cr-Co coatings. The characteristic reflections of 304 SS correspond to planes (111), (200), and (220), according to JCPDS card no. 33-0397, which are denoted with the letter A. The XRD pattern of 304 SS SB shows a characteristic peak of $SiO_2$ (incrustations produced during the sandblasting of the substrates, letter B), according to JCPDS card no. 33-1161.

The XRD pattern of the Cu coating corresponds to metallic Cu (JCPDS card no. 04-0836, letter C), with peaks located at 43.3°, 50.4°, and 74.8°, corresponding to the planes (111), (200), and (220) of Cu, respectively [30]. The XRD patterns of the Ni coating, letter D, show the characteristic reflections of Ni (JCPDS card no. 04-0850), located at 44.5°, 51.9°, and 76.5°, corresponding to planes (111), (200), and (220) of the face-centered cubic structure of metallic Ni. In the case of the Cr-Co coating, the peak located at 44° corresponds to plane (110), while the peaks located at 48° and 65° correspond to the planes (211) and (200), respectively, of metallic Cr (letter E) [31]. In the XRD pattern of the Cr-Co coating, the peak located at 34.4° corresponds to plane (009) of a double hydroxide of Cr and Co [32] (letter F). In the same XRD pattern, the peak located at 36.2° corresponds to plane (311) of Co oxide, letter G, JCPDS card no. 80-1538. Finally, the peak located at 78° corresponds to plane (602) of Cr oxide, letter H, JCPDS card no. 12-5590. These results confirm the compositions of the coatings assumed from the analysis via SEM/EDS that was carried out.

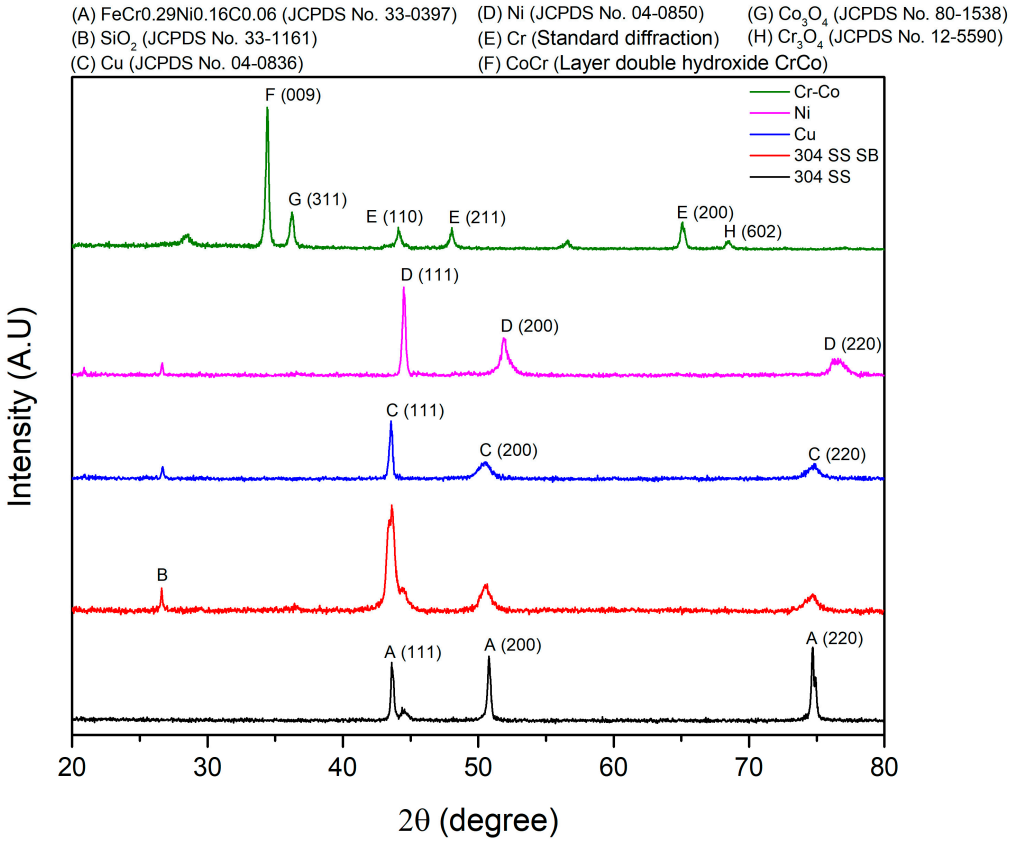



**Figure 5.** XRD patterns obtained for 304 SS (black line), 304 SS SB (red line), Cu over 304 SS SB (blue line), Ni over Cu (pink line), and Cr-Co over Ni (green line).

### *3.3. Microstructural and Cross-Sectional Analysis of Coatings*

Figure 6 shows the SEM micrographs obtained for Cr-Co oxide coatings obtained using the EG-$H_2O$ solvent. The Cu coating electrodeposited at −1.25 V is irregular, so that in the valleys higher concentrations of Fe, Cr, oxygen, and Si are detected, which come from the surface of the substrate (304 SS SB), while in the ridges a higher proportion of metallic Cu is detected. The morphology of the Cu coating is characterized by dendritic and branched patterns. The Ni coating electrodeposited at −1.40 V shows agglomerations of particles of this metal [33]. The Cr-Co oxide coating electrodeposited at −1.00 V using the EG-based solvent with the addition of water as a secondary HBD (Cr-Co:EG-$H_2O$) shows a needle-like morphology, which is characteristic of the $Co_3O_4$ oxide [34], as well as spherical particles located between the needle-like features, which are associated with the presence of metallic Cr [35]. The oxidized compounds present in this coating (Cr-Co) were

identified in the XRD patterns of Figure 5, as well as via elemental mapping of the Cr-Co coating cross section.

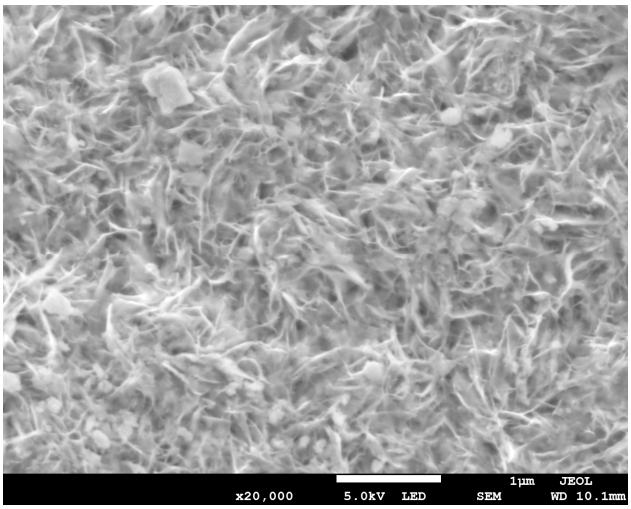
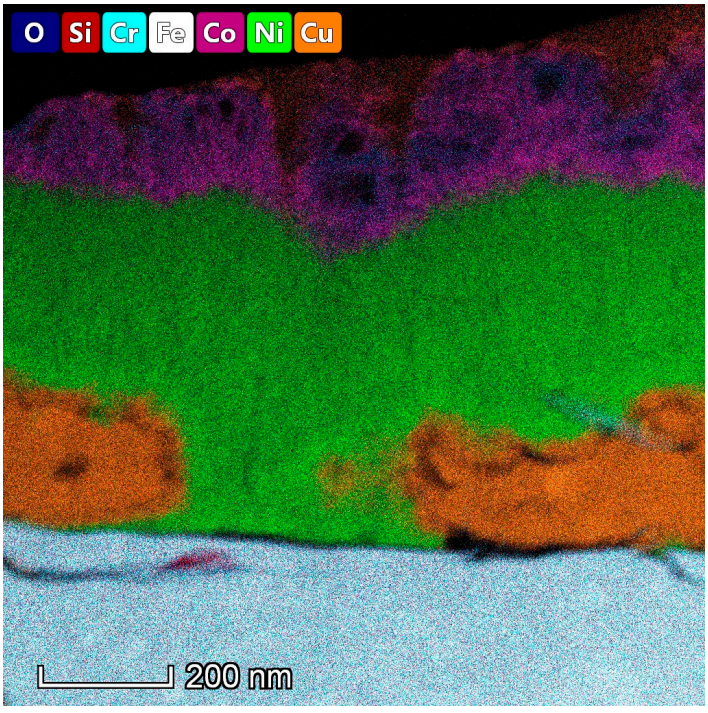


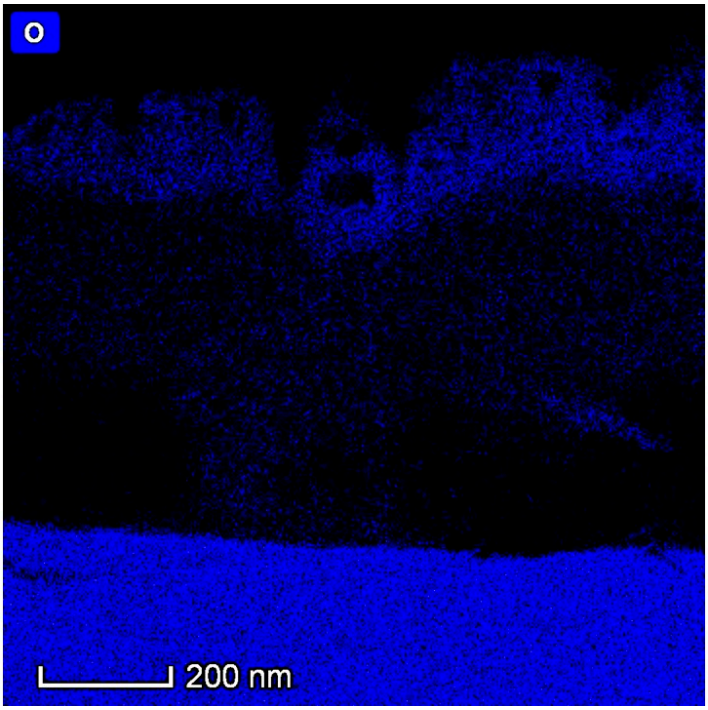

**Figure 6.** SEM micrograph of Cr-Co oxide coating obtained using the EG-$H_2O$ solvent.

The elemental mapping of the cross-section of the Cu, Ni, and Cr-Co coatings, layer upon layer, is shown in Figure 7a. Sandblasted 304 SS is coated with Cu; as this is not a uniform coating, it leaves uncovered areas on the surface of the substrate. However, when metallic Ni was electrodeposited, the entire surface was covered. After depositing the metallic coatings of Cu and Ni, the Cr-Co coating was co-deposited on top of them. The presence of oxygen was detected only in the electrodeposited Cr-Co oxide layer (Figure 7b). The average thickness of the Cu coating was 0.2 μm, the average thickness was 0.5 μm for the Ni coating, and the average thickness was about 0.3 μm for the Cr-Co coating.




(**a**)

**Figure 7.** *Cont.*




(**b**)

**Figure 7.** Elemental mapping of the cross-section of the coatings. (**a**) Cu (orange) on 304 SS SB (light blue), Ni (green), and Cr-Co oxide coating (Purple + dark blue + magenta) obtained using the EG-$H_2O$ solvent, and (**b**) O as dark blue in Cr-Co oxide coating.

### *3.4. Analysis of the Surface Wettability of Coatings*

Table 4 and Figure 8 show the results of the wettability of the 304 SS, 304 SS SB, Cu, Ni, Cr-Co:EG, and Cr-Co:EG-$H_2O$ surfaces using ultra-pure water. Contact-angle magnitudes greater than 150° indicate that the substrate surface exhibits superhydrophobic properties [36]. The evaluation of the wettability of the coatings using ultra-pure water indicated that the Cr-Co:EG-$H_2O$ coating is superhydrophobic. In contrast, the Cu, Ni, and Cr-Co:EG coatings are hydrophobic, while the 304 SS and 304 SS SB substrates are hydrophilic. Since the free surface energy varies in an inverse way to the contact angle, the greater the contact angle, the lower the energy needed to hold together the molecules of the material. This trend can be clearly seen in Table 4. This means that superhydrophobic surfaces create a water-repellent barrier, a desirable property in materials exposed to seawater.

**Table 4.** Contact angle (θ) and surface free energy determined for ultra-pure water on 304 SS, 304 SS SB, and Cu on 304 SS SB, Ni on Cu, Cr-Co:EG on Ni, and Cr-Co:Eg-$H_2O$ on Ni.

| Substrate | θ | Free Surface Energy (J/cm$^2$) | Type of Wettability |
|---|---|---|---|
| 304 SS | 37.13° | 49.68 | Hydrophilic surface |
| 304 SS SB | 67.61° | 40.83 | |
| Cu | 141.97° | 15.97 | |
| Ni | 149.40° | 14.42 | Hydrophobic surface |
| Cr-Co:EG | 147.04° | 14.24 | |
| Cr-Co:EG-$H_2O$ | 158.41° | 12.94 | Superhydrophobic surface |

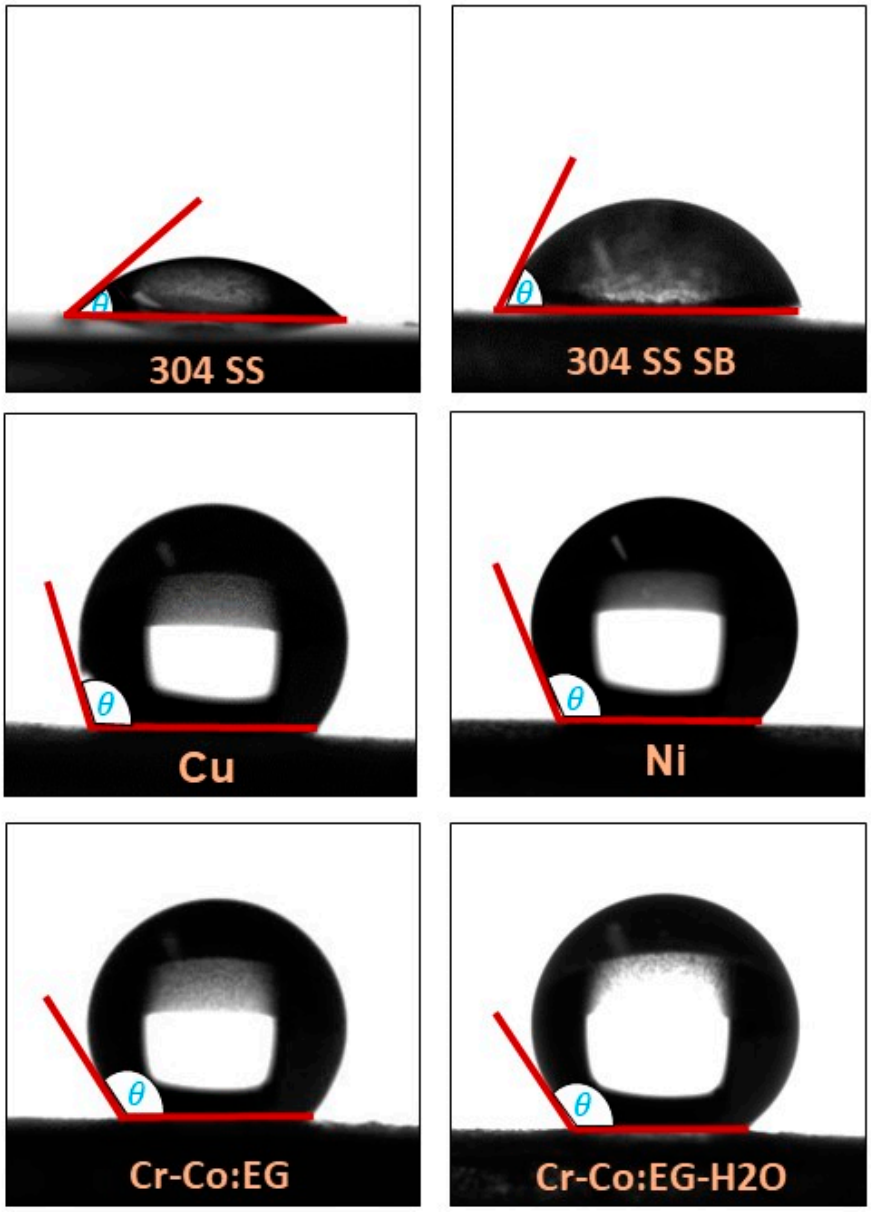



**Figure 8.** Depiction of contact angle (θ) determined for ultra-pure water on 304 SS, 304 SS SB, and Cu on 304 SS SB, Ni on Cu, Cr-Co:EG on Ni, and Cr-Co:Eg-$H_2O$ on Ni.

### *3.5. Corrosion Testing of Coatings*

The influence of Cr-Co oxide coatings on both pitting and uniform corrosion of AISI 304 SS was assessed by the CPP and EIS methods, respectively.

Pitting corrosion

From the CPP curves (Figure 9), the potentials characterizing the passivity of stainless steel were determined [37]:

- Corrosion potential, $E_{corr}$ (potential difference between a metal and an electrolyte in which the metal corrodes).
- Pitting potential, $E_{pit}$ (potential difference between a metal and an electrolyte in which the metal corrodes, is the potential at which the current density increases drastically); and
- Repassivation potential, $E_{rep}$ (potential in which a metal that has been corroded is passive again).

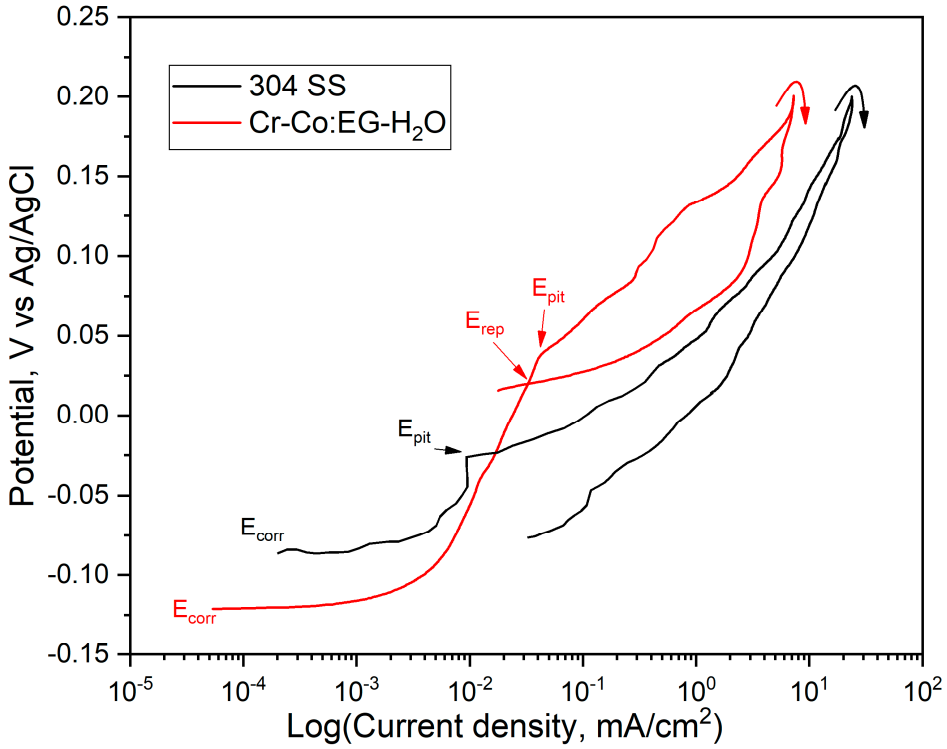



**Figure 9.** CPP curves of untreated AISI 304 SS (black line) and Cr-Co:Eg-H2O coating (red line).

By means of the first two parameters it is possible to determine the pitting corrosion resistance, $R_{pit}$, which is given by Equation (1) and whose units are mV [38,39].

$$R_{pit} = |E_{corr} - E_{pit}| \quad (1)$$

Table 5 shows the values of these parameters, which were defined in Figure 9. The surface of steel with the Cr-Co:EG-$H_2O$ coating showed greater resistance to pitting corrosion (123.93 mV) compared to untreated stainless steel (62.3 mV). This increase in corrosion resistance is due to the presence of chromium and cobalt oxides with needle-like morphology (see Figure 6), which makes it more thermodynamically stable. Another factor is the decrease in surface energy, which inhibits contact with simulated seawater thanks to the formation of a superhydrophobic surface (see Figure 8).

**Table 5.** Most important values obtained from the CPP tests.

| Coating | $E_{corr}$, mV | $E_{pit}$, mV | $R_{pit}$, mV | $E_{rep}$, mV | Hysteresis | Specific Mass Loss mg/cm$^2$ |
|---|---|---|---|---|---|---|
| Untreated 304 SS | −85.2 | −22.9 | 62.30 | 0 | None | 0.0102 |
| Cr-Co:EG-$H_2O$ | −121.11 | 36.02 | 157.13 | 24.31 | + | 0.0012 |

According to Figure 9 and Table 5, the CCP test showed a hysteresis behavior only in the case of the coated sample Cr-Co:EG-$H_2O$. The sample of untreated AISI 304 SS did not present hysteresis, which implies a low passivity against localized corrosion (pitting and cracking) [40–42]. In the coated sample the sweep lines in both directions cross at $E_{rep}$. The coated sample showed a large area of hysteresis, which is associated with high resistance to pitting corrosion. This phenomenon was due to the formation of an oxide film on the surface of the stainless steel, which caused the occurrence of a repassivation of the sample at a $E_{rep}$ value of 24.31 mV, which was beneficial since the protective passive layer on the surface of the stainless steel was restored [43,44]. Finally, the mass loss for untreated AISI 304 SS was 0.01 mg/cm$^2$ after the CPP corrosion test (black bar in Figure 10). Under the

same conditions, the coated sample Cr-Co:EG-$H_2O$ only lost 0.001 mg/$cm^2$ (red bar in Figure 10), which confirmed a greater resistance to pitting corrosion.

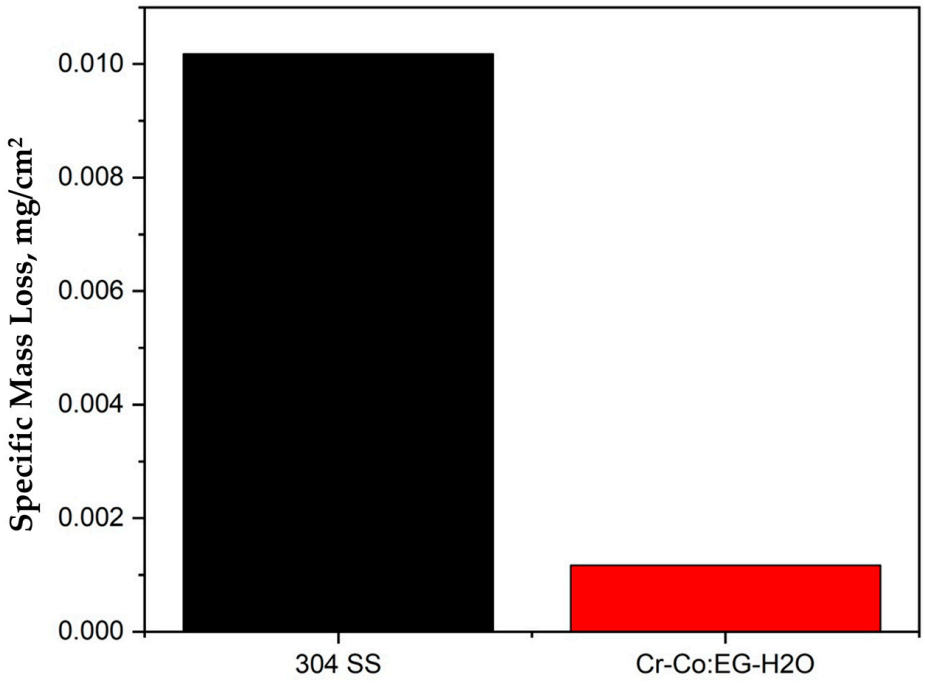



**Figure 10.** Mass loss behavior of 304 SS and Cr-Co:Eg-H2O after the CPP tests.

Uniform Corrosion

EIS has emerged as a highly relevant tool for analyzing uniform corrosion processes, owing to its capability to discriminate between interfaces and coatings [45]. Within this context, two distinct electrical circuits have been identified [46]: $R_s$ (CPE||$R_{ct}$) for application on uncoated metals, and $R_s$ ($CPE_1$||$R_{pore}$) ($CPE_2$||$R_{ct}$) for cases where a passive oxide layer or a porous coating is present on the surface. In the first equivalent circuit, $R_s$ refers to the solution resistance (simulated seawater), CPE represents the element encapsulating the capacitive properties of the electrolyte/metal interface, and $R_{ct}$ is identified as the corresponding resistance. On the other hand, in the second equivalent circuit, $CPE_1$ denotes the capacitance of the coating, while $CPE_2$ encompasses the capacitive properties of the electrolyte/metal interface, and $R_{pore}$ is established as the coating resistance [46].

This approach offers a more precise and detailed characterization of the electrochemical processes involved in corrosion, enabling a deeper comprehension of interactions at the metal-coating interface.

Figure 11 displays the Nyquist plots (impedance spectra) corresponding to the analyzed samples. These plots show the distinctive behavior patterns of both the untreated metal (AISI 304 SS) and the oxide coating (Cr-Co:EG-$H_2O$), respectively. Furthermore, the circuits used to capture the associated quantitative data are presented. Table 6 summarizes the results of the comparison between the uniform corrosion of the untreated AISI 304 SS sample (35 kΩ$cm^2$) with respect to the coated sample Cr-Co:EG-$H_2O$ (57 kΩ$cm^2$). This improvement in uniform corrosion resistance was attributed to the protection provided by the chromium and cobalt oxides obtained using an ethylene glycol-water solution (Cr-Co:EG-$H_2O$).

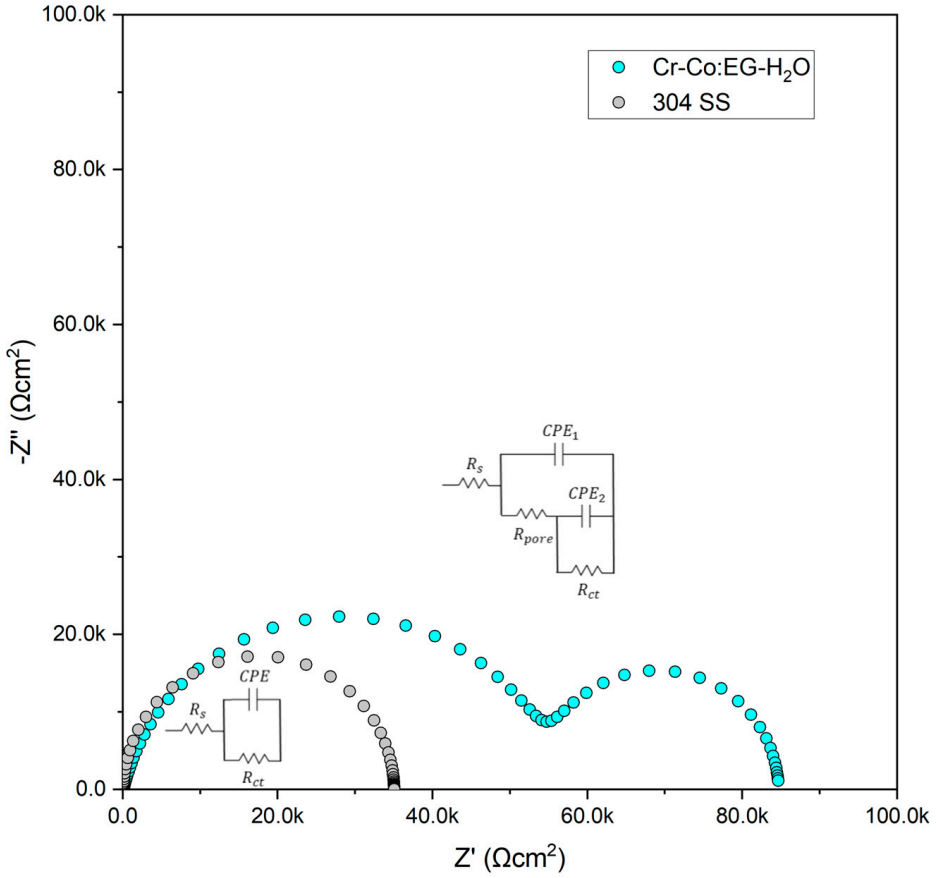



**Figure 11.** Nyquist diagrams of the EIS measurements conducted on the untreated AISI 304 SS and Cr-Co:Eg-H2O coating.

**Table 6.** Comparison of corrosion resistance obtained from EIS measurements.

| Surface | $R_s$ ($\Omega cm^2$) | $R_{ct}$ ($\Omega cm^2$) | $R_{pore}$ ($\Omega cm^2$) |
|---|---|---|---|
| Untreated 304 SS | 100 | 34,952 | - |
| Cr-Co:EG-$H_2O$ | 100 | 28,110 | 56,488 |

## 4. Conclusions

A thin layer of Cr-Co was electrodeposited at −1.00 V on top of a previously electrodeposited metallic Ni layer, using an EG-based electrolyte with water added as a secondary HBD (EG:$MCl_n \cdot YH_2O$:$H_2O_{HBD}$).

The use of ethylene glycol-water-based solvents resulted in easy control of the Cr/Co ratio of both metal and oxide species.

The oxidative effect of water added to the EG allowed us to obtain a black Cr-Co coating, as metals and oxides. Surface analysis and cross-sectional elemental mapping of the coatings confirmed this.

Ethylene glycol proved to be a suitable solvent for the electrodeposition of metallic coatings of Cu at −1.25 V and Ni on Cu at −1.40 V as undercoats to improve the adhesion of Cr-Co oxide coatings subsequently electrodeposited on top of the 304 SS surface. It also promotes a reduction in the wear rate of the coatings.

From the surface wettability and corrosion resistance analyses of the Cr-Co oxide coatings, it was found that these coatings significantly enhanced the pitting and uniform corrosion resistance of the AISI 304 SS in simulated seawater. This performance was associated with the chemical nature, morphology and superhydrophobic character of the Cr-Co coatings.

Overall, these findings strongly suggest that thin Cr-Co oxide coatings represent a promising way to enhance the durability and performance of 304 SS in marine environments.

**Author Contributions:** Conceptualization, G.V.-G.; Investigation, C.E.V.-G. and F.J.M.-B.; Methodology, G.V.-G.; Writing—original draft, C.E.V.-G.; Writing—review & editing, G.V.-G. and J.L.-C. All authors have read and agreed to the published version of the manuscript.

**Funding:** This research was funded by the Consejo Nacional de Ciencia y Tecnología (Project 2019-845101).

**Data Availability Statement:** The original contributions presented in the study are included in the article material, further inquiries can be directed to the corresponding authors.

**Acknowledgments:** We wish to express our gratitude to the National Council of Humanities, Science and Technology (CONAHCYT) for their support through the Frontier Science Project 2019-845101, "Accelerated Discovery of Antibiofouling Materials". C.E.V.-G. also thanks CONAHCYT for a Ph.D. scholarship granted to her.

**Conflicts of Interest:** The authors declare no conflict of interest.

## References

1. Sebastián, P.; Vallés, E.; Gómez, E. Copper electrodeposition in a deep eutectic solvent. First stages analysis considering Cu(I) stabilization in chloride media. *Electrochim. Acta* **2014**, *123*, 285–295. [CrossRef]
2. Abbott, A.P.; Ballantyne, A.; Harris, R.C.; Juma, J.A.; Ryder, K.S. A Comparative Study of Nickel Electrodeposition Using Deep Eutectic Solvents and Aqueous Solutions. *Electrochim. Acta* **2015**, *176*, 718–726. [CrossRef]
3. Valverde, P.; Green, T.; Roy, S. Copper Electrodeposition from a Water-Containing Choline Chloride Based Deep Eutectic Solvent. *ECS Trans.* **2017**, *77*, 859–864. [CrossRef]
4. Rao, S.; Zou, X.; Wang, S.; Lu, Y.; Shi, T.; Hsu, H.Y.; Xu, Q.; Lu, X. Electrodeposition of Ni-Cu alloy films from nickel matte in deep eutectic solvent. *Mater. Chem. Phys.* **2019**, *232*, 6–15. [CrossRef]
5. Vilková, M.; Płotka-Wasylka, J.; Andruch, V. The role of water in deep eutectic solvent-base extraction. *J. Mol. Liq.* **2020**, *304*, 112747. [CrossRef]
6. Hansen, B.B.; Spittle, S.; Chen, B.; Poe, D.; Zhang, Y.; Klein, J.M.; Horton, A.; Adhikari, L.; Zelovich, T.; Sangoro, J.R. Deep Eutectic Solvents: A Review of Fundamentals and Applications. *Chem. Rev.* **2021**, *121*, 1232–1285. [CrossRef]
7. Panzeri, G.; Accogli, A.; Gibertini, E.; Rinaldi, C.; Nobili, L.; Magagnin, L. Electrodeposition of high-purity nanostructured iron films from Fe (II) and Fe (III) non-aqueous solutions based on ethylene glycol. *Electrochim. Acta* **2018**, *271*, 576–581. [CrossRef]
8. Elsharkawya, S.; Hammad, S.; El-hallaga, I. Electrodeposition of Ni nanoparticles from deep eutectic solvent and aqueous solution promoting high stability electrocatalyst for hydrogen and oxygen evolution reactions. *J. Solid State Electrochem.* **2022**, *26*, 1501–1517. [CrossRef]
9. Vorobyova, T.N.; Vrublevskaya, O.N. Electrochemical deposition of gold–tin alloy from ethylene glycol electrolyte. *Surf. Coat. Technol.* **2010**, *204*, 1314–1318. [CrossRef]
10. Panzeri, G.; Muller, D.; Accogli, A.; Gibertini, E.; Mauri, E.; Rossi, F.; Nobili, L.; Magagnin, L. Zinc electrodeposition from a chloride-free non-aqueous solution based on ethylene glycol and acetate salts. *Electrochim. Acta* **2019**, *296*, 465–472. [CrossRef]
11. Panzeri, G.; Accogli, A.; Gibertini, E.; Varotto, S.; Rinaldi, C.; Nobili, L.; Magagnin, L. Electrodeposition of cobalt thin films and nanowires from ethylene glycol-based solution. *Electrochem. Commun.* **2019**, *103*, 31–36. [CrossRef]
12. Vargas, G.; Lopez, J.; García, A.; Cerda, J. Electrodeposition of Co-Cr Black Coatings on Steel in Deep Eutectic Solvents, for Solar Collection Applications. In Proceedings of the 11th ISES EuroSun Conference, Palma de Mallorca, Spain, 12–14 October 2016. [CrossRef]
13. Pallaro, M.; Moretto, F.L.; Panzeri, G.; Magagnin, L. Sn-Cu codeposition from a non-aqueous solution based on ethylene glycol for wafer-bonding applications: Direct and pulse electroplating. *Trans. IMF* **2018**, *96*, 265–268. [CrossRef]
14. Shaibuna, M.; Theresa, L.V.; Sreekumar, K. A New Green and Efficient Brønsted: Lewis Acidic DES for Pyrrole Synthesis. *Catal Lett.* **2018**, *148*, 2359–2372. [CrossRef]
15. Khomami, M.N.; Danaee, I.; Attar, A.A.; Peykari, M. Kinetic and thermodynamic studies of AISI 4130 steel alloy corrosion in ethylene glycol-water mixture in presence of inhibitors. *Met. Mater. Int.* **2013**, *19*, 453–464. [CrossRef]
16. Danaee, I.; Khomami, M.N.; Attar, A.A. Corrosion behavior of AISI 4130 steel alloy in ethylene glycol–water mixture in presence of molybdate. *Mater. Chem. Phys.* **2012**, *135*, 658–667. [CrossRef]
17. *ISO/TC 156*; Corrosion of Metals and Alloys. ISO: Geneva, Switzerland, 1974. Available online: https://www.iso.org/committee/53264.html (accessed on 27 June 2023).
18. *ISO 12944-2*; Paints and Varnishes—Corrosion Protection of Steel Structures by Protective Paint Systems—Part 2: Classification of Environments. ISO: Geneva, Switzerland, 2017. Available online: https://www.iso.org/standard/64834.html (accessed on 27 June 2023).
19. Tsustumi, Y.; Doi, H.; Nomura, N.; Ashida, M.; Chen, P.; Kawasaki, A.; Hanawa, T. Surface Composition and Corrosion Resistance of Co-Cr Alloys Containing High Chromium. *Mater. Trans.* **2016**, *57*, 2033–2040. [CrossRef]

20. Serafin, D.; Nowak, W.J.; Wierzba, B. The effect of surface preparation on high temperature oxidation of Ni, Cu and Ni-Cu alloy. *Appl. Surf. Sci.* **2019**, *476*, 442–451. [CrossRef]
21. Yetik, O.; Koçoğlu, H.; Avcu, Y.Y.; Avcu, E.; Sinmazcelik, T. The Effects of Grit Size and Blasting Pressure on the Surface Properties of Grit Blasted Ti6Al4V Alloy. *Mater. Today Proc.* **2020**, *32*, 27–36. [CrossRef]
22. Hammond, O.S.; Bowron, D.T.; Edler, K.J.; Hammond, S.; Edler, K.J.; Bowron, D.T. The Effect of Water upon Deep Eutectic Solvent Nanostructure: An Unusual Transition from Ionic Mixture to Aqueous Solution. *Angew. Chem. Int. Ed.* **2017**, *56*, 9782–9785. [CrossRef]
23. *ISO 11130*; Corrosion of Metals and Alloys—Alternate Immersion Test in Salt Solution. ISO: Geneva, Switzerland, 2017. Available online: https://www.iso.org/standard/71867.html (accessed on 27 June 2023).
24. ASTM G61-86 (Reapproved 2018)-Standard Test Method For Conducting Cyclic Potentiodynamic Polarization Measurements For Localized Corrosion Susceptibility of Iron-, Nickel-, Or Cobalt-Based Alloys. 2018. Available online: https://www.astm.org/g0061-86r18.html (accessed on 1 September 2023).
25. Wang, Z.; Wu, T.; Ru, J.; Hua, Y.; Bu, J.; Wang, D. Eco-friendly preparation of nanocrystalline Fe-Cr alloy coating by electrodeposition in deep eutectic solvent without any additives for anti-corrosion. *Surf. Coat. Technol.* **2021**, *406*, 126636. [CrossRef]
26. Li, W.; Hao, J.; Mu, S.; Liu, W. Electrochemical behavior and electrodeposition of Ni-Co alloy from choline chloride-ethylene glycol deep eutectic solvent. *Appl. Surf. Sci.* **2020**, *507*, 144889. [CrossRef]
27. Ramos-Lora, N.; Mendoza-Huizar, L.H.; Reyes, C.H.R. Cobalt electrodeposition onto stainless steel 304 from ammoniacal solutions. *J. Chil. Chem. Soc.* **2011**, *56*, 631–634. [CrossRef]
28. Wellings, J.S.; Samantilleke, A.; Heavens, S.; Warren, P.; Dharmadasa, I. Electrodeposition of CuInSe 2 from ethylene glycol at 150 °C. *Sol. Energy Mater. Sol. Cells* **2009**, *93*, 1518–1523. [CrossRef]
29. Neuróhr, K.; Pogány, L.; Tóth, B.G.; Révész, Á.; Bakonyi, I.; Péter, L. Electrodeposition of Ni from Various Non-Aqueous Media: The Case of Alcoholic Solutions. *J. Electrochem. Soc.* **2015**, *162*, D256–D264. [CrossRef]
30. Soliz, A.; Alfaro, C.; Cáceres, L.; Guzman, D. Morphological characterization of copper deposited by electrolysis influenced by presence of chloride ions. *Rev. Mater.* **2021**, *26*. [CrossRef]
31. Quan, C.; He, Y. Properties of nanocrystalline Cr coatings prepared by cathode plasma electrolytic deposition from trivalent chromium electrolyte. *Surf. Coat. Technol.* **2015**, *269*, 319–323. [CrossRef]
32. Dong, C.; Yuan, X.; Wang, X.; Liu, X.; Dong, W.; Wang, R.; Duan, Y.; Huang, F. Rational design of cobalt–chromium layered double hydroxide as a highly efficient electrocatalyst for water oxidation. *J. Mater. Chem. A* **2016**, *4*, 11292–11298. [CrossRef]
33. Costovici, S.; Manea, A.C.; Visan, T.; Anicai, L. Investigation of Ni-Mo and Co-Mo alloys electrodeposition involving choline chloride based ionic liquids. *Electrochim. Acta* **2016**, *207*, 97–111. [CrossRef]
34. Sulciute, A.; Baltrusaitis, J.; Valatka, E.; Valatka, E. Structure, morphology and electrochemical properties of zinc-cobalt oxide films on AISI 304 type steel. *J. Appl. Electrochem.* **2015**, *45*, 335–345. [CrossRef]
35. Meena, S.P.; Ashokkumar, R.; Kumar, E.R. Effects of Cr Doping Concentration on Structural, Morphology, Mechanical and Magnetic Properties of Electrodeposited NiCoCr Thin Films. *J. Inorg. Organomet. Polym. Mater.* **2018**, *29*, 1094–1099. [CrossRef]
36. Liu, E.; Yin, X.; Hu, J.; Yu, S.; Zhao, Y.; Xiong, W. Fabrication of a biomimetic hierarchical superhydrophobic Cu-Ni coating with self-cleaning and anti-corrosion properties. *Colloids Surf. A Physicochem. Eng. Asp.* **2020**, *586*, 124223. [CrossRef]
37. Pedeferri, P.; Ormellese, M. *Corrosion Science and Engineering*; Springer: Berlin/Heidelberg, Germany, 2018. Available online: https://www.google.com.sg/books/edition/Corrosion_Science_and_Engineering/uNdvDwAAQBAJ?hl (accessed on 17 August 2023).
38. El Kacimi, Y.; Kaya, S.; Touir, R. *New Challenges and Industrial Applications for Corrosion Prevention and Control*; IGI Global: Hershey, PA, USA, 2020; pp. 1–304. [CrossRef]
39. Videla, H.A. Prevention and control of biocorrosion. *Int. Biodeterior. Biodegrad.* **2002**, *49*, 259–270. [CrossRef]
40. McCafferty, E. *Introduction to Corrosion Science*; Springer Science & Business Media: Berlin, Germany, 2010; pp. 1–575. [CrossRef]
41. Abdel Hameed, R.S.; Abdallah, M. Corrosion Inhibition of Carbon Steel in 1 M Hydrochloric Acid using Some Pyrazolo[3,4-d]Pyrimidnone Derivatives. *Prot. Met. Phys. Chem. Surf.* **2018**, *54*, 113–121. [CrossRef]
42. Esmailzadeh, S.; Aliofkhazraei, M.; Sarlak, H. Interpretation of Cyclic Potentiodynamic Polarization Test Results for Study of Corrosion Behavior of Metals: A Review. *Prot. Met. Phys. Chem. Surf.* **2018**, *54*, 976–989. [CrossRef]
43. Ovarfort, R. Critical pitting temperature measurements of stainless steels with an improved electrochemical method. *Corros. Sci.* **1989**, *29*, 987–993. [CrossRef]
44. Silverman, D.C. Tutorial on Cyclic Potentiodynamic Polarization Technique. *Corrosion* 1998. Available online: https://api.semanticscholar.org/CorpusID:92343669 (accessed on 1 September 2023).
45. Orazem, M.E.; Tribollet, B. A tutorial on electrochemical impedance spectroscopy. *ChemTexts* **2020**, *6*, 2. [CrossRef]
46. ALópez-Ortega; Arana, J.L.; Bayón, R. Tribocorrosion of Passive Materials: A Review on Test Procedures and Standards. *Int. J. Corros.* **2018**, *2018*, 7345346. [CrossRef]


**Disclaimer/Publisher's Note:** The statements, opinions and data contained in all publications are solely those of the individual author(s) and contributor(s) and not of MDPI and/or the editor(s). MDPI and/or the editor(s) disclaim responsibility for any injury to people or property resulting from any ideas, methods, instructions or products referred to in the content.